Onset of three dimensional flow instabilities in lid-driven circular cavities

L.M. González,* E. Ferrer,† and H.R. Díaz-Ojeda*

(Dated: June 14, 2017)

Three-dimensional instabilities for two circular lid-driven cavities are investigated by linear stability analysis and Direct Numerical Simulations using high order spectral techniques. Two circular geometries have been analysed and compared: a circular cavity with an horizontal top boundary and a circular cavity with circular lid. Compared to more classic results for squared and rectangular lid driven cavities, the corners of these rounded geometries have been partially or totally removed. Critical Reynolds numbers, neutral curves and three dimensional structures associated to the least stable modes have been identified by linear stability analysis and then confirmed by spectral Direct Numerical Simulations.

We show that the geometries that present fewer sharp corners have enhanced stability: the circular cavity with a flat lid presents the first bifurcation at $(Re_c, k_c) \approx (1362, 25)$ whilst the circular lid bifurcates at $(Re_c, k_c) \approx (1438, 18)$, where Re_c is the critical Reynolds number based on the cavity diameter and lid tangential velocity, and k_c is the spanwise wavenumber. Neutral curves and properties of the leading three dimensional flow structures are documented and analogies to instabilities in other lid-driven cavities discussed. Additionally, we include results for the adjoint problem and structural sensitivity 3D iso-maps (i.e. wavemaker regions), to show that the cavity corners play a relevant role in the generation of 3D instabilities.

I. INTRODUCTION

Flows in lid-driven cavities have occupied fluid mechanics research for decades, from a theoretical, numerical and experimental point of view. Unlike flow instabilities in simply squared shape and rectangular containers, which are by now fairly well understood, relatively less work is available for three-dimensional lid-driven cavities that present rounded boundaries. The present contribution addresses, from a computational point of view, three-dimensional flow instabilities in lid-driven cavities of different cross-sections that are totally or partially rounded. The reader interested in a review of internal re-circulating flows in square and rectangular cavities generated by the motion of one or more of the container walls is referred to the classic text of Shankar and Deshpande [45], who discussed aspects such as corner eddies, longitudinal vortices, laminar-turbulent transition and turbulence flows in cavities. Since the year 2000, when the review was published, many efforts have contributed to provide new results on such flows. Here, we provide a short review of relevant results to situate the present work in the appropriate context.

By far the most quoted two-dimensional numerical simulations of square lid-driven cavity flow are from Ghia [22] and Schreiber and Keller [44], who obtained a range of solutions for $Re \leq 10000$. These results have served as benchmark for numerical simulations of incompressible solvers during that decade and beyond. Two and three dimensional instabilities observed in numerical and experimental flows in rectangular cavities are fairly well

understood in the context of linear global flow instability [15, 48]. It is accepted that centrifugal instabilities arise from two dimensional steady flows to generate three dimensional structures in lid-driven square cavities [1, 3, 24] and open cavities [6, 11, 37]. However, elliptical instabilities have been reported for lid-driven rectangular or doubly lid-driven cavities[1, 3, 24]. Additionally, it is important to mention that in cavity flows, the first bifurcation is associated to a three dimensional instability. Note that this is not the case for wake flows, such as cylinders, where the first instability is two dimensional and leads to a von Karman Street.

Regarding bifurcations in the square cavity restricted to two-dimensional flow, the interested reader is referred to [5, 7, 40]. To date, the range of critical Reynolds numbers predicted for two-dimensional (spanwise wavenumber parameter $k = 0$) global flow instability, $Re_{2d,crit} \in [7400, 8375]$, is wide enough to warrant further work. Three-dimensional global instabilities of spanwise homogeneous square lid-driven cavity flows have been analysed in [14] and (independently) in [46] and [3]. In contrast to the wide range of critical conditions of two-dimensional flow instability, substantially better agreement exists in the literature regarding the critical Reynolds number associated to the three-dimensional modes in the square lid-driven cavity [1, 3, 49].

Turning away from regular rectangular domains, a number of theoretical predictions exist in (two-dimensional) cavities of complex two-dimensional profiles. Most researchers have studied cavities with polygonal cross sections. Two-dimensional flow in a trapezoidal cavity, permitting lid motion of the unequal trapezium sides and documenting the respective steady flow patterns in the Reynolds number range $Re \in [100, 1000]$ have been reported [12]. The same trapezoidal lid-driven cavity flow, as well as flow in an equilateral triangular cavity, was solved in the range $Re \in [1, 500]$[36], while [42] ad-

---

* School of Naval Engineering, Universidad Politécnica de Madrid, Avda. Arco de la Victoria 4 28040 Madrid Spain
† School of Aeronautics, Universidad Politécnica de Madrid, Plaza del Cardenal Cisneros s/n 28040 Madrid Spain

dressed the equilateral triangular lid-driven cavity flow in the same Reynolds number range. Three-dimensional biglobal instability of a lid-driven cavity of equilateral triangular shape was analysed by the finite-element method on unstructured grids to predict the leading part of the eigenspectrum and the critical Reynolds number for the three-dimensional instability at ($\mathrm{Re}_c \approx 1870, k_c \approx 6.73$)[28]. An interesting extension is the study of lid-driven cavities of isosceles triangular shape is performed in [26], where both flow directions were studied and the agreement between the numerical results and the experiments was remarkable. Several lid-driven cavity geometries of complex two-dimensional cross sectional profile may be built by superposition of rectangular domains. The two most representative cases discussed in the literature are the L-shaped cavity, introduced in [17, 38, 39], and the two-box-cavity proposed in [29]. It is interesting to note that linear stability analysis have shown that three-dimensional instabilities (and their onset) are highly dependent on the two-dimensional shape of the cavity. Biglobal instability of the L-shaped, two-box and cross-shaped versions have been addressed in [17] and [13]. In the former, the enhanced stability obtained when rounding the corner of the L-shaped cavity was demonstrated and analysed through sensitivity analyses.

The cited work defines biglobal analysis when: the baseflow velocity field has two or three components that only depend on two spatial coordinates, and perturbations with three velocity-components that depend on three spatial coordinates. Additionally, the biglobal analysis assumes a harmonic dependence on one homogeneous direction. For flows with a homogeneous direction, three-dimensional stability analysis can be decomposed using normal modes (Fourier components), reducing significantly the computational cost.

This assumption, does not allow the study of end-wall effects. However, as summarised by Kuhlmann and Albensoeder [32], walls are only important for short spanwise lengths, since end-wall effects driven by Bödewadt flow decay exponentially from walls. Consequently, the flow at the centre of the cavity, even if end effects are considered, is identical to periodic spanwise cavities of infinite span.

Very little work has been done when part of the perimeter of the cross sections of the cavity is rounded. In [41], the flow in an elliptic region with a moving boundary is described. The stability analysis of lid-driven cavity flow in a two-dimensional domain using a stream function-vorticity formulation of a quarter-circular cross-section was presented in [50], who reported steady flow patterns for $Re \in [0, 1000]$. Some issues encountered in the last work, related with the singularities in the boundary conditions at the moving-lid endpoints, were overcome in [31] and [21]. The latter made use of triangular grids in which corners do not require special treatment.

In the present work, we explore two lid-driven cavity flows developing in three-dimensional containers having circular or partially circular cross sectional profiles and one homogeneous spatial direction. The flow is driven by the motion of part of the perimeter. To the authors's knowledge this work is novel and presents linear stability analysis of geometries that have not been studied in the past. Furthermore, the text explores the destabilising effect of geometrical corners in the onset of three dimensional instabilities. In order to provide a deeper description of the role of the cavity perimeter in the physics that control the stability, we extend the linear global stability analysis to provide adjoint modes. The combination of direct and adjoint modes enables the detection of the regions with maximum structural sensitivity, i.e. the wavemaker region [23, 34] and relates to the origin of absolute instabilities. The sensitivity analysis is provided for both circular cavities and may be compared to published results for rectangular shapes [24].

The rest of the paper is organised as follows. In the formulation section II, the geometry and boundary conditions for the circular cavities are introduced. In the mathematical models section III, the numerical methodologies are described, whilst the results section IV describes and discusses results of base flow calculations and subsequent linear stability analysis. Additionally, the linear stability results are compared with Direct Numerical Simulations. Finally, the main findings are summarised in the conclusion section V.

II. PROBLEM SETUP

The primary objective of the paper is to evaluate the impact on the flow stability when the perimeter of a square cavity is transformed by removing corners. The critical stability parameters of two rounded cavities have been analysed and compared to the classic square lid-driven cavity. In these new designs, the moving part of the boundary driving the flow will be referred as Γ_1 and the no slip boundary as Γ_2, such that the complete boundary is $\Gamma = \Gamma_1 \bigcup \Gamma_2$.

The first cavity (i.e. with a horizontal flat lid), referred henceforth as *PCavity*, is the result of intersecting a circle of radius $R = 1/2$ (and diameter $d = 1$) centred at $(x, y) = (0, 0)$ with an horizontal plane placed (the lid) at $y = R\sin(\pi/4)$ above the centre of the circle. The flow is generated as the lid moves parallel to the positive x-axis, see figure 1. Compared to the square lid-driven cavity, the two bottom corners have been removed, the bottom and vertical boundaries have been rounded, but the lid driving top plane remains. The intersection between the circle and the top boundary creates two points $(\pm\sqrt{2}/4, \sqrt{2}/4)$ that define the moving boundary plane, where a regularised boundary condition is applied:

$$u(\Gamma) = \begin{cases} 1 - (\frac{4x}{\sqrt{2}})^{18} & in \quad \Gamma_1, \\ 0 & in \quad \Gamma_2, \end{cases} \qquad (1)$$
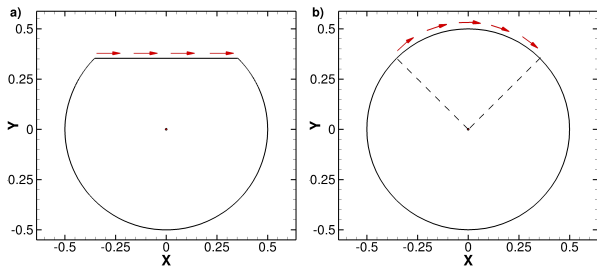
FIG. 1: Geometries of the circular cavities using dimensionless coordinates. The centre of the cavities is at $x = 0$ and $y = 0$ and the lid moves as indicated in red. a) *PCavity*, circular cavity with flat top horizontal lid that moves parallel to the x-axis and b) *CCavity*, circular cavity with a top $90°$ arc lid that moves clockwise in the azimuthal direction.

being the vertical velocity component v zero at Γ.

A second circular cavity (i.e. with a circular lid), referred henceforth as *CCavity*, is also analysed. The upper quarter arc of the cavity drives the flow tangentially clockwise, see figure 1. To study the influence of the corners in the flow stability, when compared to the square lid-driven cavity and the *PCavity*, all walls have been rounded and corners removed. The *CCavity* has a constant tangential velocity at the moving boundary Γ_1, where the regularised expression used for the lid boundary is:

$$\mathbf{u}(\Gamma) = \begin{cases} \left(1 - (\frac{4x}{\sqrt{2}})^{18}\right)\mathbf{u}_t & in \quad \Gamma_1, \\ 0 & in \quad \Gamma_2, \end{cases} \quad (2)$$

where $\mathbf{u}_t = (y/R, -x/R)$ is the unitary tangential velocity vector.

III. MATHEMATICAL MODELS

A. Stability analysis

Linear stability analysis is presented in this section. The geometry and the coordinate system are shown in figure 1. The geometry and the boundary conditions enable two-dimensional steady flow in the (x,y)-plane. We are interested in the development of three dimensional flow structures upon the steady two-dimensional flow. This study requires two steps. First, we compute a two-dimensional steady flow and second we analyse the evolution of the perturbations upon the flow computed in the first step.

The flow is governed by the incompressible Newtonian Navier-Stokes equations in a domain Ω bounded by Γ. The non-dimensional version of this set of equations reads:

$$\frac{\partial \boldsymbol{u}}{\partial t} + \boldsymbol{u} \cdot \nabla \boldsymbol{u} = -\nabla p + \frac{1}{\text{Re}}\nabla^2\boldsymbol{u}, \quad (3a)$$

$$\nabla \cdot \boldsymbol{u} = 0. \quad (3b)$$

Here, we non-dimensionalised using d, d/U, U, and ρU^2 for length, time, velocity and pressure, respectively, where $d = 2R$ is the cavity diameter and U the lid velocity. The fluid has density ρ and kinematic viscosity ν. The Reynolds number is defined as $\text{Re} = \frac{Ud}{\nu}$.

1. Steady laminar base flows

The problem allows a steady two-dimensional base state $(\boldsymbol{u}_0, p_0)(\boldsymbol{x}) \equiv (u_0, v_0, w_0, p_0)(x, y)$ with $w_0 = 0$, $\partial/\partial t = 0$. This steady flow must satisfy the base-state equations

$$\boldsymbol{u}_0 \cdot \nabla \boldsymbol{u}_0 = -\nabla p_0 + \frac{1}{\text{Re}}\nabla^2\boldsymbol{u}_0, \quad (4a)$$

$$\nabla \cdot \boldsymbol{u}_0 = 0, \quad (4b)$$

subject to boundary conditions $u_0 = v_0 = 0$ on the stationary walls. The flow is driven by the motion of the lid as explained in the previous section II.

To compute the base flows for stability analysis, two independent methods have been used. On the one hand, we use the high order spectral element code Nektar [9], which is known for its exponential (or spectral) convergence. On the other hand, and for validation purposes, we compute the base flow by time-integration of (4), using the semi-Lagrangian finite element solver ADFC [27] developed by the first author. In both solvers, the time integration is started from a state of rest $[(\boldsymbol{u}_0, p_0)(t = 0) = 0]$ and terminated when the criterion

$$\max_j\{|g_j(t + \Delta t) - g_j(t)|\} < 10^{-12} \quad (5)$$

is satisfied, g_j being the local value of any flow quantity at any node j and Δt the step size for the time integration.

The classical lid-driven cavity when the lid moves with constant velocity can be considered as a singular mathematical problem as the velocity boundary conditions are discontinuous on both ends of the moving lid. Depending on the cavity studied, we numerically employ the regularised boundary conditions given by the equations 1 and 2, in which the lid-velocity is filtered as in [33] as an alternative to the constant velocity formulation. To clarify the negligible effect of the numerical regularisation of the boundary conditions on the global flow and its stability some comparison were presented in [26] for a isosceles triangular cavity.

2. Linear stability: eigenvalue-problem formulation and solution methodology

Since we are interested in the linear stability of the two-dimensional steady base flow, we consider perturbations

$(\tilde{\boldsymbol{u}}, \tilde{p})$ such that the total flow fields are

$$\boldsymbol{u} = \boldsymbol{u}_0 + \tilde{\boldsymbol{u}}, \tag{6a}$$

$$p = p_0 + \tilde{p}. \tag{6b}$$

Substituting (6) into (3) and linearising with respect to $\tilde{\boldsymbol{u}}$, the perturbation equations are obtained:

$$\frac{\partial \tilde{\boldsymbol{u}}}{\partial t} + \boldsymbol{u}_0 \cdot \nabla \tilde{\boldsymbol{u}} + \tilde{\boldsymbol{u}} \cdot \nabla \boldsymbol{u}_0 = -\nabla \tilde{p} + \frac{1}{\mathrm{Re}} \nabla^2 \tilde{\boldsymbol{u}}, \tag{7a}$$

$$\nabla \cdot \tilde{\boldsymbol{u}} = 0, \tag{7b}$$

The perturbation flow must satisfy the no-slip boundary conditions $\tilde{\boldsymbol{u}} = 0$ on Γ. Since the coefficients of (7) do not depend on z and t the perturbations quantities can be written as normal modes

$$\tilde{\boldsymbol{u}} = \hat{\boldsymbol{u}}(x,y) \mathrm{e}^{\gamma t + \mathrm{i}kz} + \text{c.c.}, \tag{8a}$$

$$\tilde{p} = \hat{p}(x,y) \mathrm{e}^{\gamma t + \mathrm{i}kz} + \text{c.c.}, \tag{8b}$$

where the complex conjugate (c.c.) is required to render the perturbations real. We are interested in the temporal stability analysis where the spanwise periodic length (i.e. homogeneous direction) L_z is defined through the real wave number $k = \frac{2\pi}{L_z} \in \mathbb{R}$. Consequently, the analysis is performed on a 2D shape that represents a 3D periodic domain with finite span L_z and harmonic variations in the z-direction. This framework does not contain any explicit z-coordinate and periodic boundary conditions are required in the spanwise direction. Additionally, $\gamma = \sigma + \mathrm{i}\omega \in \mathbb{C}$ is the complex growth/decay rate σ and oscillation frequency ω.

Substitution of the ansatz (8) into the perturbation equations (7) yields

$$\left(\mathcal{L} + \frac{\partial u_0}{\partial x} \right) \hat{u} + \hat{v} \frac{\partial u_0}{\partial y} + \frac{\partial \hat{p}}{\partial x} = -\gamma \hat{u}, \tag{9a}$$

$$\left(\mathcal{L} + \frac{\partial v_0}{\partial x} \right) \hat{v} + \hat{u} \frac{\partial v_0}{\partial x} + \frac{\partial \hat{p}}{\partial y} = -\gamma \hat{v}, \tag{9b}$$

$$\mathcal{L}\hat{w} + \mathrm{i}k\hat{p} = -\gamma \hat{w}, \tag{9c}$$

$$\frac{\partial \hat{u}}{\partial x} + \frac{\partial \hat{v}}{\partial y} + \mathrm{i}k\hat{w} = 0, \tag{9d}$$

where $\mathcal{L}$ is the linear advection-diffusion operator:

$$\mathcal{L} = u_0 \frac{\partial}{\partial x} + v_0 \frac{\partial}{\partial y} - \frac{1}{\mathrm{Re}} \left(\frac{\partial^2}{\partial x^2} + \frac{\partial^2}{\partial y^2} - k^2 \right). \tag{10}$$

For the present case of a base flow velocity vector $(u_0, v_0, 0)^{\mathrm{T}}$ normal to the wave vector $k\boldsymbol{e}_3$ it is possible to define a real eigenvalue problem (thus halving the memory requirements for its solution) by re-defining the out-of-plane velocity component [47] such that $\hat{w} \to -\mathrm{i}\hat{w}$. Note that for simplicity, we do not change the symbol for $\hat{w}$ in what follows. This converts system (9) into a real generalised eigenvalue problem:

$$A \cdot \boldsymbol{X} = -\gamma B \cdot \boldsymbol{X}, \tag{11}$$

where $\boldsymbol{X} = (\hat{u}, \hat{v}, \hat{w}, \hat{p})^{\mathrm{T}}$ with real linear operators A and B. The eigenvalues γ of such a real eigenvalue problem are either real or they arise as pairs of complex conjugate eigenvalues. Adopting the existing nomenclature from the literature, see e.g. Theofilis et al. [49], the corresponding eigenvectors describe either stationary modes ($\gamma = 0$) or travelling waves ($\gamma = \pm \mathrm{i}\omega \neq 0$).

To discretise the equations, we use a triangular-element-based unstructured mesh, since it is ideally suited for our geometries, further details as well as the entries of all matrices are presented in the appendix of [28]. The eigenvalue problem is solved using a Krylov-subspace iteration, originally proposed by [43] and discussed in detail in [30, 47]. The typical leading dimension of the matrix A is $\mathrm{DIM}(A) \equiv 3N_u + N_p = O(7 \times 10^4)$, where N_u and N_p are the numbers of quadratic velocity- and linear pressure-nodes, respectively. Sparse linear-algebra algorithms have been used in order to obtain the LU-decomposition necessary within the Arnoldi method, which permits storing only the $O(9 \times 10^6)$ non-zero elements of this matrix. The total time needed for a complete Arnoldi analysis depends, on the one hand, on the efficiency of the linear solver, and on the other hand, on the Krylov space dimension m used to approximate the leading eigenvalues. In this case the size of the Krylov space dimension used and consequently the number of eigenvalues computed by the Arnoldi algorithm is $m = 100$. We should also remark that no shift parameter has been used for these calculations. In order to check the accuracy of the results during the stability analysis, the polynomial order of the approximation P was increased until three significant digits of the most unstable eigenvalue were converged.

A similar approach can be extended to calculate the adjoint counterparts but solving the adjoint system of equations [4]. A comparison of the direct and discrete approaches to compute direct and adjoint modes can be found in recent work [25]. Regarding adjoint methods for hydrodynamic stability, an overview of recent developments has been compiled in [34]. The regions where the direct and adjoint modes overlap define the structural sensitivity to localised feedback or wavemaker regions[23]. These sensitivity maps provide information on the flow regions where a generic force-velocity coupling causes the largest drift in the eigenvalues and hence provides useful information on control strategies to attenuate these instabilities [8, 23, 34]. Other flow sensitivities, e.g. to base flow modification or steady forcing [35], have been defined in the literature but are not considered here.

B. Spectral Direct Numerical Simulations

Direct Numerical Simulation (DNS) do not require modeling and hence can be used for validation of linear stability results. This code is based on primitive variables, where (u, v, w) will be the velocity components

and p the pressure. Here, the non-linear 3D incompressible Navier-Stokes equations are solved using an unsteady high order ($order \geq 3$) H/P discontinuous Galerkin - Fourier solver developed by the second author and detailed in [16, 18–20]. This high order solver provides highly accurate solutions on static and moving meshes composed of mixed triangular-quadrilateral meshes and can cope with curved boundary elements as required to compute flows in circular cavities.

A second order stiffly stable method is used to discretise the NS equations in time whilst spatial discretisation is provided by the discontinuous Galerkin - Symmetric Interior Penalty Galerkin formulation with modal basis functions in the x-y plane. Spatial discretisation in the z-direction is provided by a purely spectral method that uses Fourier series and allows computation of spanwise periodic three-dimensional flows. The solver has been widely validated for a variety of flows, including bluff body flows, airfoil and blade aerodynamics under static and rotating conditions [16, 19, 20] and global instability analysis [17].

High order (≥ 3) numerical methods (e.g. Spectral, discontinuous Galerkin) have seen an increased popularity over the last decade. They are characterised by low numerical errors (i.e. dispersion and diffusion) and their ability to use mesh refinement (H-refinement) and/or polynomial enrichment (P-refinement) in order to achieve accurate solutions. Polynomial enrichment provides exponential decay of the error for smooth solutions as opposed to the typical constant decay provided by the H-refinement strategy. This enables the P-refinement strategy to reach the same level of accuracy with fewer degrees of freedom. Reviews of the main advantages of high order Discontinuous Galerkin methods in the context of aeronautical applications can be found in [51].

All Direct Numerical Simulations use a non-dimensional time step $\triangle t = 0.002$ and with the regularised boundary conditions for the lid described previously, (1) for the *PCavity* and (2) for the *CCavity*. We initialise all flow components to zero and allow the flow to develop. Once the 2D flow is converged, we introduce random white noise (with small amplitudes) to all flow components. For unstable flows, we can observe exponential growth of third velocity component with same growth and frequency predicted by linear stability analysis. If the flow is stable, we see exponential decay of the introduced disturbances. Although our DNS simulations include non-linear terms, the analysis is limited to small three dimensional perturbations such that it is almost equivalent to an analysis performed using a linearised solver. Note that we never allow saturation of the three dimensional flow. In our experience, non-linear simulations agree very well with instability analysis when perturbations are small and before non-linear saturation appears. Additional comparisons between linearised, non-linear DNS and global stability analysis may be found in previous work [17].

C. Computational Meshes

This section describes the final meshes (after preliminary convergence tests) retained for the stability analysis and DNS computations. Convergence tests are included in an Annex of this work, section VI.

PCavity for stability analysis: The first mesh created to study the *PCavity*, mesh M1, is a typical finite element mesh conformed by 7509 $P2 - P1$ Taylor-Hood triangular elements and 15730 quadratic velocity nodes. This mesh is used for computation with the semi-Lagrangian finite element, and has a number of degrees of freedom per velocity component equivalent to the number of nodes $dof_{2d} = 15730$.

A second mesh M2, was used to confirm the mesh independence of the results. The mesh M2 was a conformed by 824 triangular spectral elements with polynomial order $P = 3$. The resulting number of degree of freedom for M2 per velocity component are $dof_{2d} = 824\frac{(P+1)(P+2)}{2} = 8240$, where we have taken into account the number of mesh elements and polynomial order inside each triangular element. This is necessary when using high order spectral methods.

CCavity for stability analysis: The unstructured spectral element mesh created to study the *CCavity* is an constituted of 576 quadrilateral elements with polynomial order $P = 3$. The polynomial order of the computations has been increased in both cavities until base flow and stability results were converged. The resulting number of degree of freedom per flow variable (velocity-component or pressure) for this mesh is $dof_{2d} = 576 \times (P + 1)^2 = 9216$.

PCavity for DNS simulations: The x-y plane for the *PCavity* uses 211 tri-quad elements of which 24 are quadrilateral elements with curved boundaries that fit exactly (through the numerical mapping [20]) the circular geometry. In all elements the numerical solution is spanned using a polynomial order P=7, such that the number of degrees of freedom per flow variable and x-y plane is $dof_{2D} = 24 \times (P + 1)^2 + 186\frac{(P+1)(P+2)}{2} = 8268$. To discretise the homogeneous dimension, we use 8 Fourier planes (5 Fourier modes) such that the overall number of degrees of freedom is $dof_{3D} = 66144$.

CCavity for DNS simulations: The x-y plane for the *CCavity* uses 228 tri-quad elements of which 32 are quadrilateral elements to fit the circular boundary condition. Again, we select a polynomial order P=7, such that the number of degrees of freedom per flow variable and x-y plane is $dof_{2D} = 32 \times (P+1)^2 + 196\frac{(P+1)(P+2)}{2} = 9104$. Using 8 Fourier planes, the overall number of degrees of freedom is $dof_{3D} = 72832$.

Let us note that the number of degrees of freedom of the DNS computations in the x-y plane agree with the meshes used for stability analysis (see section 5). However, DNS computations require 3D meshes, which increase considerably the cost of the simulations. This shows the advantage of performing biglobal stability

analysis, where all computations are two-dimensional avoiding the high computational cost of performing three dimensional computations.

IV. RESULTS

In this section the results obtained using the direct and adjoint formulations of the linear global stability analysis are presented and compared with spectral DNS computations. For the two circular cavities, both the baseflow and the stability analysis will be presented. Steady two-dimensional flows are stable at sufficiently small Reynolds numbers. Note that the existence of a 2D steady state implies stability for spanwise wavenumber $k = 0$ or for infinite axial length $L_z = \infty$.

The solutions of these eigenvalue problems provide a general framework for the prediction of the onset of flow instability and the detection of the structural sensitivity for both cavities.

To provide context to this study, we summarise the critical values found in the literature for other cavities. Namely, the square cavity becomes unstable to 3D perturbations, consequently showing exponential growth in the spanwise velocity component at $Re_c = 782.61$ and $k_c = 15.37$, the L-shaped cavity at $Re_c = 650$ and $k_c = 9.7$ and the isosceles triangular at $Re_c = 540.2$ and $k_c = 2.86$ or $Re_c = 780$ and $k_c = 10.5$ depending on the flow direction. Additionally, we remind the reader that when the geometries present sharp corners (e.g. squares, rectangles or triangles) and sufficiently large Reynolds numbers are considered, then the flow streamlines show small recirculating regions near the corners that shape the large centred recirculating region inside the cavity (see [26, 28, 45] for illustrations).

A. Flat Lid Cavity: *PCavity*

Figures 2 and 3 show the velocity and vorticity contours for the baseflow at supercritical conditions for $Re = 1400$ for the *PCavity*. In contrast to what occurs in square or triangular cavities (that have corners, narrow angles and associated small recirculating regions [26, 28]), no presence of secondary vortices in the top corners are identified in this new geometry and only the presence of a centred dominant vortex and centred near the cavity centre can be observed.

In table I, the baseflow computed by the two different computational methods (described in section 2) are compared. The tabulated data have been obtained using a low order finite element method and a high order H/P-spectral method both using a time marching method until the convergence criteria is satisfied. The table shows good agreement between the two solvers. Minor discrepancies are attributed to the different nodal points used by each numerical method that locate maxima and minima at slightly different places. The maximum
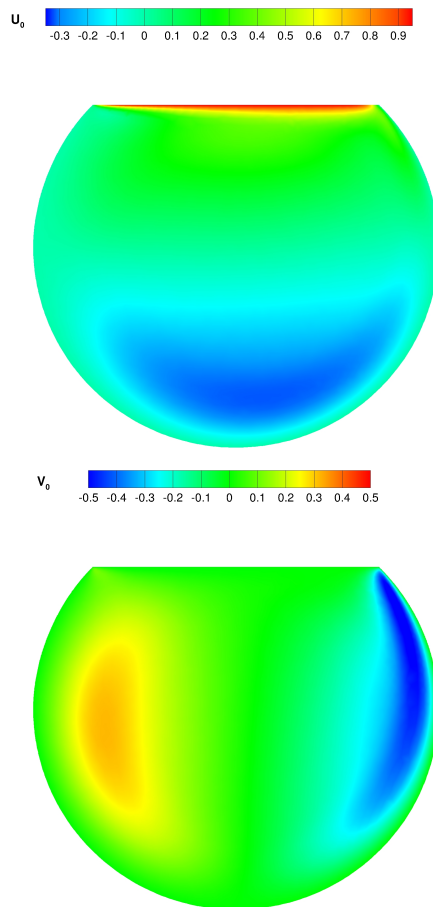

FIG. 2: *PCavity* baseflow velocity components at $Re = 1400$. Top: Horizontal component u_0. Bottom: Vertical component v_0.
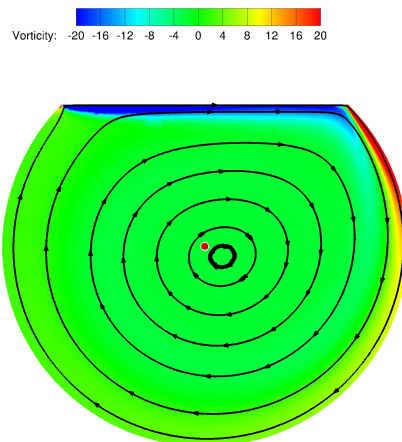

FIG. 3: *PCavity* baseflow vorticity and 7 streaklines at $Re = 1400$. The red dot indicates the cavity centre.

TABLE I: Extrema of the base flow velocity field for Re = 1400 and the respective (x, y)-coordinates for the regularised *PCavity*.

	Low order FEM	High order spectral h-p
$\min u_0$	-0.3741	-0.3730
$x^{\min u_0}$	0.0693	0.0686
$y^{\min u_0}$	-0.3763	-0.3750
$\max v_0$	0.3224	0.3197
$x^{\max v_0}$	-0.3247	-0.3225
$y^{\max v_0}$	-0.0397	-0.0396
$\min v_0$	-0.5505	-0.5500
$x^{\min v_0}$	0.3936	0.3899
$y^{\min v_0}$	0.2677	0.2674

difference is about 1% which occurs for the x coordinate of maximum of the u_0 in table I, showing that our results are mesh converged and independent of the numerical method selected.

For base flow calculations, a time-step $\Delta t = 0.01$, was used. This value yields moderate total run times. As an example, we show in figure 4, the base flow velocity components along lines $y = 0$ and $x = 0$ for both methods employed. It can be seen that the results for both methods are in excellent agreement.

For numerical efficiency, the stability analysis has been carried out varying the wave number $k = \frac{2\pi}{L_z}$ in discrete steps of 0.5. As an example, we show the growth rate $\sigma(k)$ in figure 5 of the least stable mode for three different Reynolds numbers $Re = 1300, 1400, 1500$. Since the resulting imaginary part corresponding to these least stable modes is zero, we conclude that the critical modes for the *PCavity* have zero frequency (curve not included) and are consequently stationary. Following the classical notation in lid driven cavity analysis, e.g. [49], the most unstable stationary mode (with zero-frequency) will be noted as S1. We also represent the second most unstable mode for the same Reynolds numbers, see figure6, that in this case is not stationary but travelling and denoted T1.

The supercritical mode S1 for $Re = 1400$ and $k = 23$ is shown in figure 7. In contrast to what happens in square, rectangular or triangular cavities, the perturbation flow field for the spanwise direction $\hat{w}$ is not located near the cavity centre where the main eddy is centred. In this case, the left side and top left corner show the dominant parts of the perturbation.

Figure 10 shows the neutral stability curves for the stationary instability, where the stability limits of the modes S1 and T1 are represented. From these calculations, we conclude that the local minimum of the neutral curve $Re(k)$ corresponds to the critical point with associated critical mode or eigenvector. The critical Reynolds and wavenumber for regularised boundary conditions are $Re_c = 1362.8$ and $k_c = 22.8$. In order to ensure that the local minimum of the neutral stability curve, is indeed the critical Reynolds number,
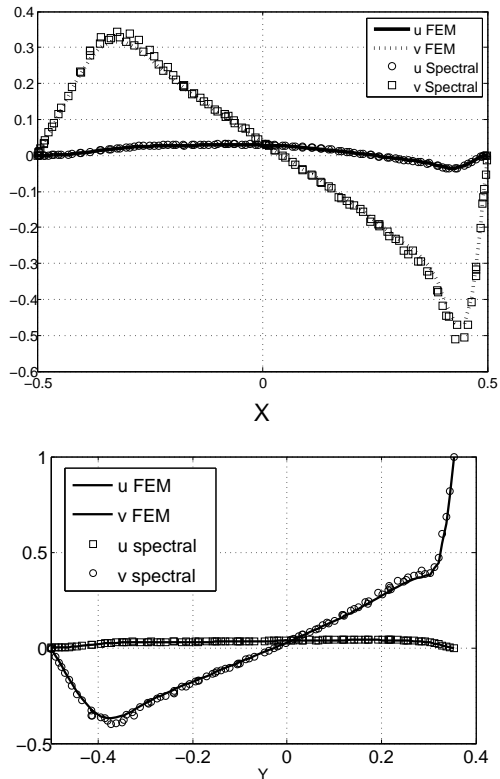

FIG. 4: Velocity components of the *PCavity* base flow at $y = 0$ (top) and $x = 0$ (bottom) for $Re = 1400$ for the low order FEM code and the spectral H/P element code.

we compute the maximum growth rate σ within the wider range $k \in [1, 30]$ for a Reynolds number fixed to $Re = 1360$. Within this extended range of wavenumbers, all modes are stable (with growth rates $\sigma < 0$). As shown in [26], the regularisation of the lid velocity has only a small effect on the critical Reynolds and wavenumbers, consequently quantitatively small changes would be expected if non-regularised boundary conditions are used.

The results obtained for the *PCavity* are in line with the predictions of [2, 46, 49] when analysing the square lid driven cavity. The critical mode is also stationary (and would consequently be impossible to detect using power-series analysis of experimental data), whilst the second is a travelling mode. It is important to underline, that similarly to what occurs in the square cavity, the critical point is detected at a large wavenumber, consequently it is important to analyse a wide range of wavenumbers to detect this point. Some previous works such as [14] missed this critical mode in the square cavity because of their limited range of wavenumbers tested.

Figure 7 depicts the shape of most untable mode for Re=1400 and $k = 23$. Similarly to what happens in the square cavity, see [49], most activity takes place
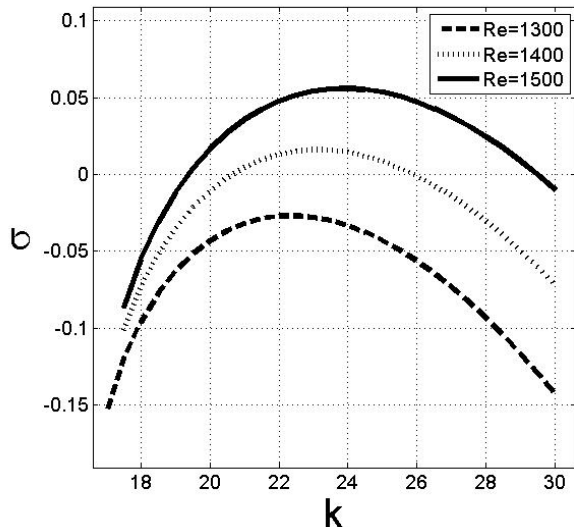
FIG. 5: Growth rates of the most unstable mode S1 versus k for different Reynolds numbers in the *PCavity*. This mode has zero angular frequency $\omega = 0$.

in the neighbourhood of the left rounded wall of the cavity (or cavity leading edge), which can be identified with the $x = 0$ wall of the square cavity. Another important similarity with the square cavity is that, when the spatial structure of the eigenfunctions of the three most unstable *PCavity* modes are compared, very few qualitative differences were found, see figure 8

According to these results, we can define the limits for two or three-dimensional simulations. It is now clear that three dimensionality will manifest itself at supercritical conditions. Two-dimensional DNS will predict a steady-state when $Re < Re_c$ whilst a three-dimensional simulation is necessary to accurately simulate the flow above Re_c, for a given $L_z = 2\pi/k$.

Observing these results, we can state that S1 is the only amplified eigenmode in the region $Re \in [1364, 1446]$; since this is a stationary mode its amplification is expected to be observed as a spanwise modulation of the steady flow, having a periodicity length related to the most unstable wavenumber by $L_z = 2\pi/k = 0.27$ cavity length/depth units. If the Reynolds number is taken in the range $Re > 1446$ the travelling mode T1 also becomes unstable. In that situation, the mode is three dimensional, consequently the complex conjugate of the T1 eigenmode is also a solution of the perturb equations (9) and the two complex-conjugate modes form a standing wave pattern which grows at the rate of T1, linearly superimposed upon the growing S1 mode [49]. The most amplified wavenumbers of S1 and T1 lie quite close to each other and the best way to differentiate those modes in the Reynolds interval $[1364, 1446]$ is measuring the frequency of the travelling mode T1.

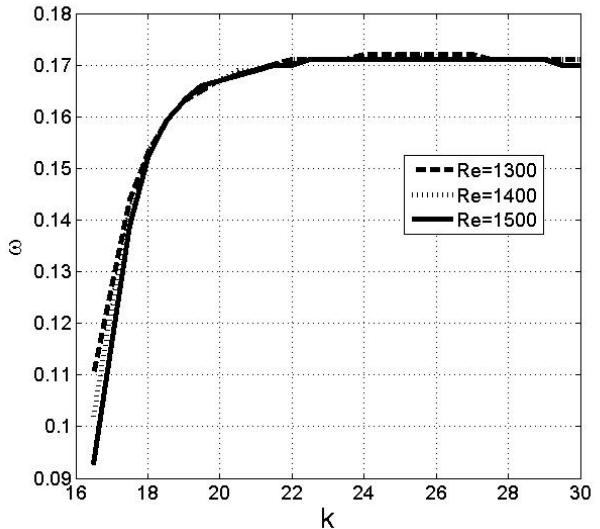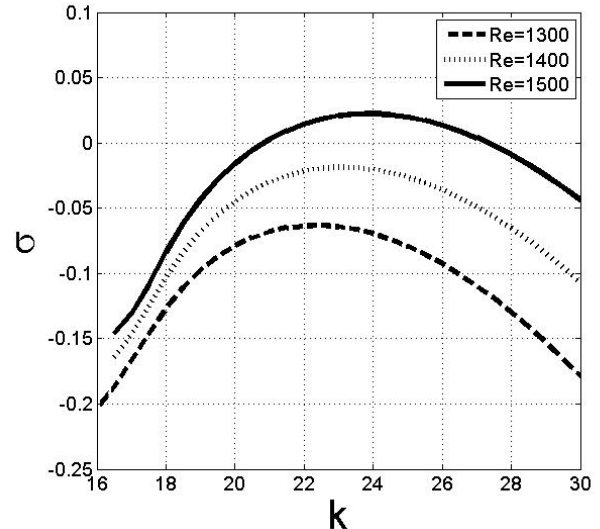In order to provide a deeper insight of the role that the

FIG. 6: Growth rates (top) and angular frequency (bottom) of the second most unstable mode T1 versus k for different Reynolds numbers in the *PCavity*.

corners are playing in the *PCavity*, an adjoint analysis has been performed and the structural sensitivity is also presented here. The real parts of the direct and adjoint most unstable eigenmode, corresponding to the axial components, and the structural sensitivity are shown in figure 7 and9. It can be observed that the adjoint mode presents an almost symmetric structure compared to the direct, that can be explained by the upstreaming advective nature of the adjoint equations [34]. In addition, the adjoint mode provides information about the flow receptivity to external forcing. The upstream nature of the mode is not surprising since it indicates the regions were an external force (i.e. momentum source) would be more influential. Comparing the adjoint mode
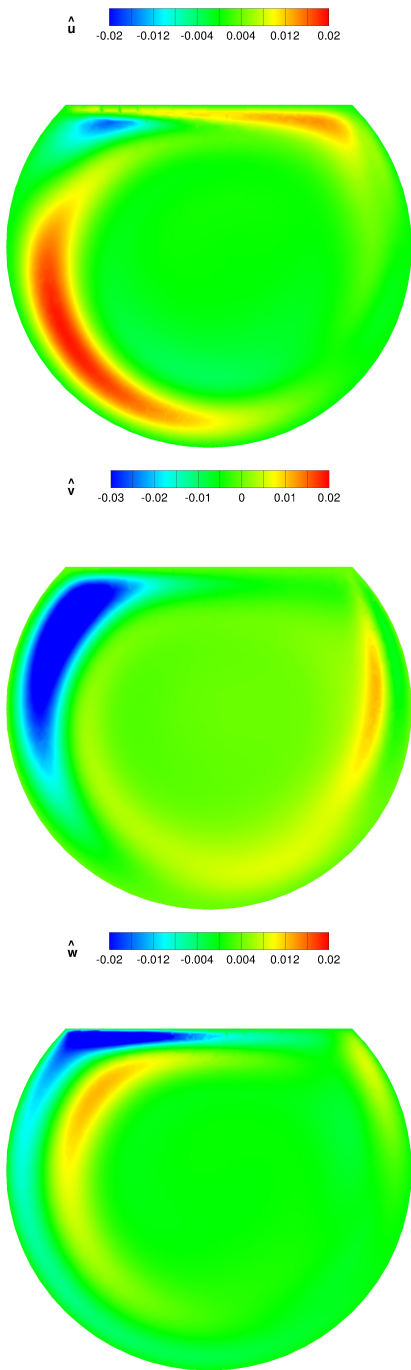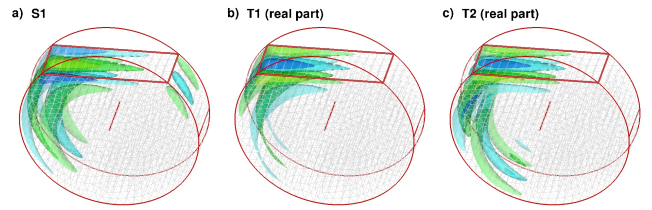
FIG. 8: Spatial distribution of the axial velocity perturbation of the three most unstable eigenmodes in the *PCavity* at $Re = 1500$ and $k = 23$. The eigenvalues are $(\sigma, \omega) = (5.4167 \times 10^{-2}, 0.0), (2.0768 \times 10^{-2}, 1.4344 \times 10^{-1}), (-6.0897 \times 10^{-2}, 2.2003 \times 10^{-2})$
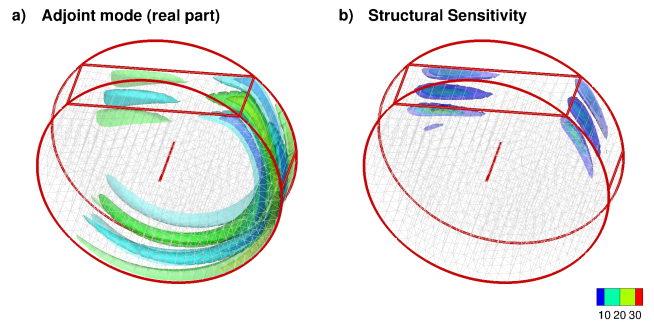

FIG. 9: *PCavity* at $Re = 1500$ and $k = 23$: a) Spatial distribution of the axial velocity perturbation of the adjoint most unstable eigenmode (associated to the direct mode S1) and b) corresponding structural sensitivity (wavemaker region).

FIG. 7: Velocity perturbation amplitudes (real parts) of the most unstable mode S1 for the *PCavity* at Re=1400 and $k = 23$. Top: $\hat{u}$, middle: $\hat{v}$ and bottom: $\hat{w}$.

to the direct mode, figures 8.a and 9.a, it can be seen that the axial component presents minimum overlap. To quantify this overlap, the structural sensitivity [23, 25] is computed and depicted in figure 9.b, thus locating the most sensitive regions of the eigenvalue problem to localised feedback (self-sustained flow oscillation or

wavemaker region). The structural sensitivity maps can be calculated using the expression $S = \|\widehat{\mathbf{w}}_{\mathbf{Adj}}\|\|\widehat{\mathbf{w}}\|$ with $< \widehat{\mathbf{w}}_{\mathbf{Adj}}, \widehat{\mathbf{w}} >= 1$, where $\widehat{\mathbf{w}}$ and $\widehat{\mathbf{w}}_{\mathbf{Adj}}$ are the direct and adjoint modes, where $< \cdot, \cdot >$ denotes the inner product, with its associated norm $\| \cdot \| =< \cdot, \cdot >^{1/2}$. The resulting sensitivity map for the *PCavity* is shown in figure 9. The localised region of sensitivity denotes the wide spatial separation between direct and adjoint modes, which is related to the non-normality [10] of the Navier-Stokes equations. Finally, the sensitivity region shows that flow modifications leading to a more stable system (i.e., flow control strategies) should be introduced in the proximities of the cavity corners, and where the moving wall modifies the flow direction leading to increased gradients. An interesting comparison with the product of the direct and adjoint modes of the square lid driven cavity performed by [24] could be made. We can observe that in the square lid driven cavity due to the presence of the bottom straight corners, the product of the direct and adjoint eigenmodes extends to the bottom part of the cavity. In the *PCavity*, when these corners are removed, the structural sensitivity shows minimum values at the lower part of the cavity and is only significant in the upper part of the cavity.

To confirm the results obtained by the global analysis, full 3D DNS simulations have been performed at different Reynolds numbers and different spanwise lengths. Initially, the spanwise component of the flow W is zero, but as the flow evolves, an exponential growth (sometimes referred to as linear growth since can be modelled using linearised equations) for the W-velocity can be detected and measured. When perturbations grow sufficiently, non-linear interactions (arising from the convective term in the Navier-Stokes equations) take over leading to the saturated non-linear regime. Then, no linear growth can be appreciated but a saturated non-linear regime. We concentrate here in the exponential part and do not show results for 3D saturated regimes. During the linear growth, the shape of the spanwise velocity component of the DNS solution can be qualitatively compared to the spanwise velocity component of the perturbation, see figure 11. When compare the DNS solution on cutting planes to the combined flow resulting from the combination of the base flow state and the scaled critical mode. Views of this combination are shown in figure 12 for two orthogonal planes at constant x=-0.35 and y=0.25. The spanwise cell formation leaves a very similar footprint on the selected planes. It is clear that both linear stability results and DNS simulations are in good agreement.
In addition, growth rates for the DNS results can be obtained by monitoring the temporal evolution of the absolute value of the W-velocity component at a point, here we select $(x/d, y/d, z/d) = (0.1, 0.1, 0.0)$. Figure 13, show clear exponential growth for both rounded cavities when monitoring the W-velocity at Re=1500 and $k = 23$. Comparing the growth rates, for the $PCavity$, issued from linear stability to the DNS results, we find similar results: $\sigma = 0.06$ for the DNS and $\sigma = 0.0542$ for the stability analysis.

Minor discrepancies are attributed to the DNS calculation, since these simulations are initialised with random white noise, allowing the Navier-Stokes system to select or filter growing/decaying perturbations. In this context, the monitored velocity even if governed by a particular flows structure, is generally polluted by slowly decaying modes. This can be seen in figure 13 for the $PCavity$, where at initial times a mode with non-zero frequency perturbs the slope (the growth) of the leading unstable mode. As time progresses, the mode with non-zero frequency decays (it is stable) such that the the slope (associated to the leading unstable mode) growths without frequency. The resulting final curve shows no clear frequency and a growth rate of 0.06. Note that if we allow longer computations, then non-linear interactions lead to a saturated regime, where linear modes have no-longer meaning. On the contrary, stability analysis discerns between flow structures and avoids overlapping effects.
Finally, let us note that we have selected a Reynolds number above the critical value, for comparison to DNS. This is related to the fact that in the limit of instability, three-dimensional perturbation grow very slowly and it would take very long to observe such flow structures. The
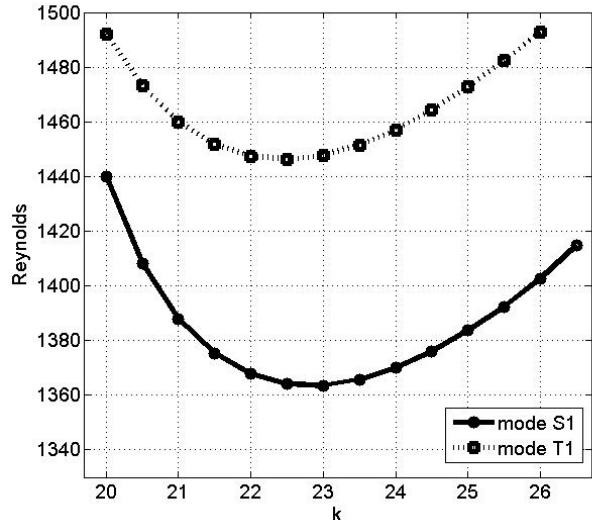

FIG. 10: Neutral stability curves for the $PCavity$ using regularised boundary conditions.

computational time shortens considerably when selecting larger growths rates (or larger Reynolds). Additional results showing convergence of the DNS simulations when varying the spanwise length are included in an Annex of this text, section VI.

B. Circular Lid Cavity: $CCavity$

As the results from the low order finite element method and the high order spectral H/P method in the $PCavity$ were very similar, in this second cavity, the baseflow computation and the subsequent analysis has been performed only using the spectral H/P element method. Figure 14 shows the contour levels of both baseflow velocity components at $Re = 1450$. The time step used during the baseflow evolution towards the stationary state is again $\Delta t = 0.01$. Figure 15 shows visualisations of the base flow state vorticity and streak lines for a supercritical Reynolds number $Re = 1450$. As the geometry is smoother than in the $PCavity$ case, and presents a complete absence of corners, no presence of secondary vortices are identified in the baseflow calculation and only the presence of a centred dominant vortex near the cavity centre is visualised. The location of the centre of the primary vortex in the $CCavity$ is placed near the cavity centre and only minor deformations of the circular trajectories are appreciated near the points where the moving boundary begins (cavity leading edge).

Table II presents characteristic values once the stationary criteria is satisfied. The value max v_0 is not represented because its maximum is found in the moving boundary. As an example, we show in figure 16, the base
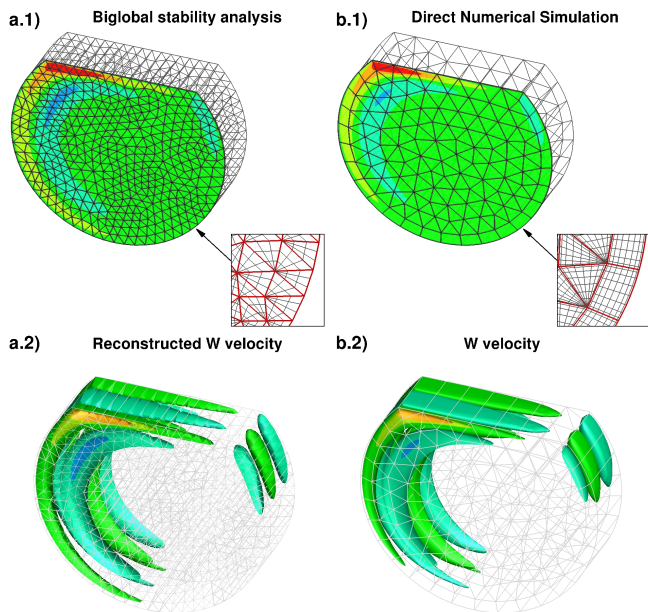
a.1) Biglobal stability analysis   b.1) Direct Numerical Simulation

a.2) Reconstructed W velocity   b.2) W velocity

FIG. 11: Comparison between the W-velocity axial velocity perturbation of the $PCavity$ at $Re = 1400$ $k = 23$: a) the linear stability analysis and b) DNS simulation. Contour maps (top) and iso-surfaces (bottom).
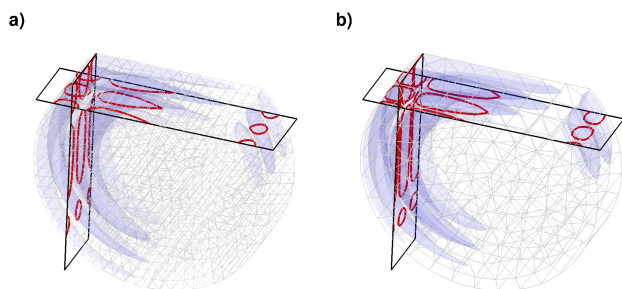

a)   b)

FIG. 12: Superposition of the base flow and the arbitrarily scaled supercritical mode at $Re = 1400$ and $k = 23$ for one wavelength of the flow in the $PCavity$: a) linear stability analysis and b) DNS simulation. The cross-sections shown are taken at $x = -0.35$ and $y = 0.25$.

TABLE II: Extrema of the base flow velocity field for Re = 1450 and the respective (x, y)-coordinates for the regularised $CCavity$.

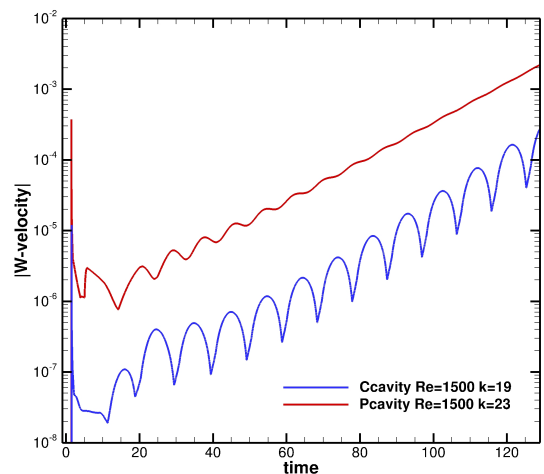| High order spectral h-p					
$\min u_0$	$x^{\min u_0}$	$y^{\min u_0}$	$\min v_0$	$x^{\min v_0}$	$y^{\min v_0}$
-0.4134	0.0646	-0.3587	-0.6309	0.3454	0.3302

FIG. 13: Direct Numerical Simulation of the temporal evolution for the absolute value of the spanwise velocity component (W-velocity) monitored at $(x/d, y/d, z/d) = (0.1, 0.1, 0.0)$. $PCavity$ (red) at $Re = 1500$ and $k = 23$ and $CCavity$ (blue) at $Re = 1500$ and $k = 19$.

flow velocity components along the lines $y = 0$ and $x = 0$. When comparing the velocity distributions for the $CCavity$, figure 16, and for the $PCavity$, figure 4, is remarkable the similarity.

The growth rate $\sigma(k)$ and the angular frequency of the least stable mode are presented in figure 17. As in the previous $PCavity$, we identify the local minimum of $Re(k)$ and the associated eigenvector that represents the critical mode.

The range of selected wavelengths is $k \in [1, 30]$. Figure 19 shows the neutral stability curve for the stationary instability of the $CCavity$; the $PCavity$ neutral curve is included for comparison. The critical Reynolds and wavenumber for regularised boundary conditions are $Re_c \approx 1438$ and $k \approx 18$. It is worth mentioning that when the critical Reynolds number of the square cavity is compared to either the $PCavity$ or the $CCavity$, see table III, this value doubles for the new geometries where some or all corners have been removed. When the critical wavelengths of the three cavities are compared, the $CCavity$ presents a similar value compared to the square, while the $PCavity$ shows a higher value. According to these results, we can confirm that when removing geometrical corners the stability of the flow inside the cavity is enhanced noticeably.

The supercritical mode at $Re = 1500$ and $k = 19$ is shown in figure 20. In contrast to what happens in rectangular and triangular cavities, the perturbation field is not significant in the centre of the cavity where main eddy is centred. Similarly, to what was observed for the $PCavity$, left side or leading edge, where the lid movement starts, concentrate the most dominant part of the spanwise perturbation component $\hat{w}$ perturbation.
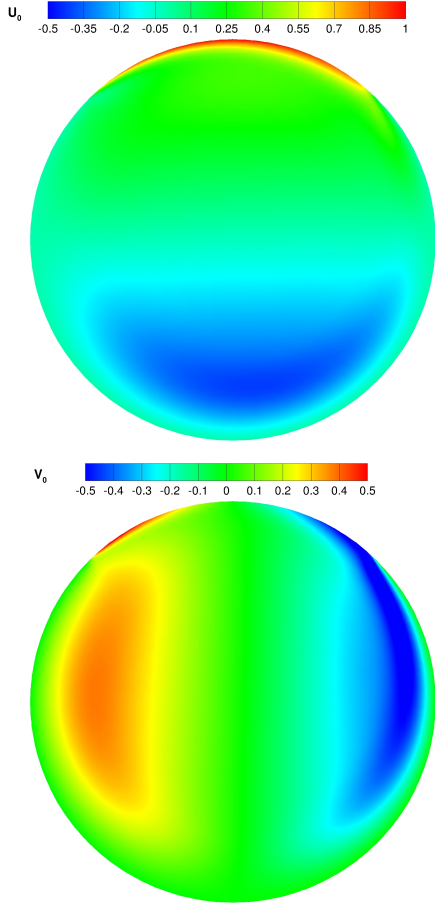
FIG. 14: CCavity baseflow velocity components at $Re = 1450$. Top: horizontal component. Bottom: vertical component.
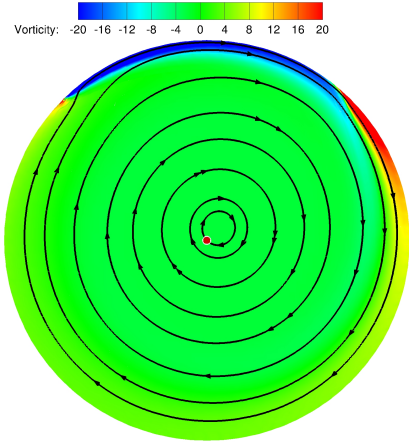

FIG. 15: CCavity baseflow vorticity and 8 streaklines at $Re = 1450$. The red dot indicates the cavity centre.
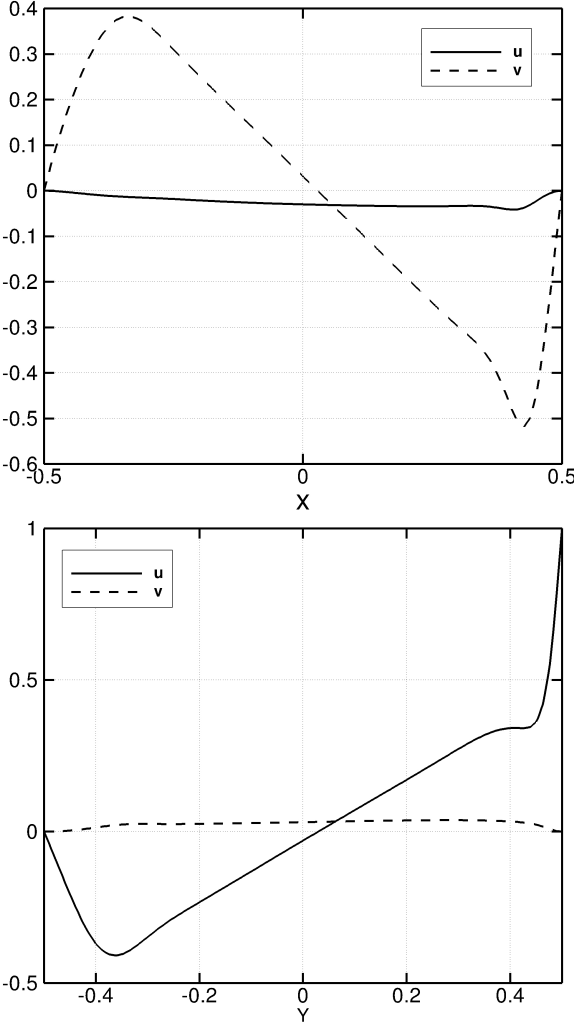

FIG. 16: Velocity components of the $CCavity$ base flow at $y = 0$ (top) and $x = 0$ (bottom) at $Re = 1450$ for the spectral H/P element code. u_0 continuous and v_0 dotted line

TABLE III: Comparison of the critical Reynolds numbers and wavelengths for the circular cavities and the square cavity [49].

	Mode S1 (Re_{crit}, k_{crit})	Mode T1 (Re_{crit}, k_{crit})
Square [49]	(782.61 , 15.37)	(844.57 , 15.77)
$PCavity$	(1362.80 , 22.80)	(1446.12 , 23.57)
$CCavity$	(- , -)	(1438.00 , 18.00)

A fundamental difference governs the stability of both rounded cavities. In the $PCavity$ the leading most unstable mode was found to be a stationary mode (without frequency), similarly to what happens in the square cavity. However, the most unstable mode governing the instability in the $CCavity$ is a travelling mode (with temporal frequency). Let us note that a
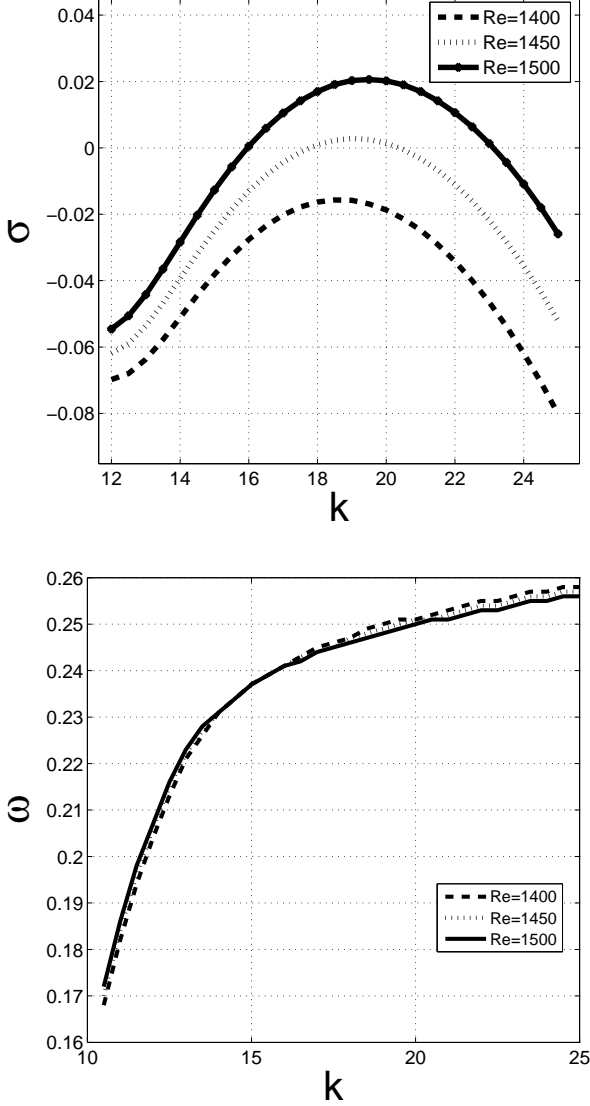
FIG. 17: Growth rates (top) and angular frequency (bottom) of the most unstable mode T1 versus k for different Reynolds numbers in the *CCavity*.
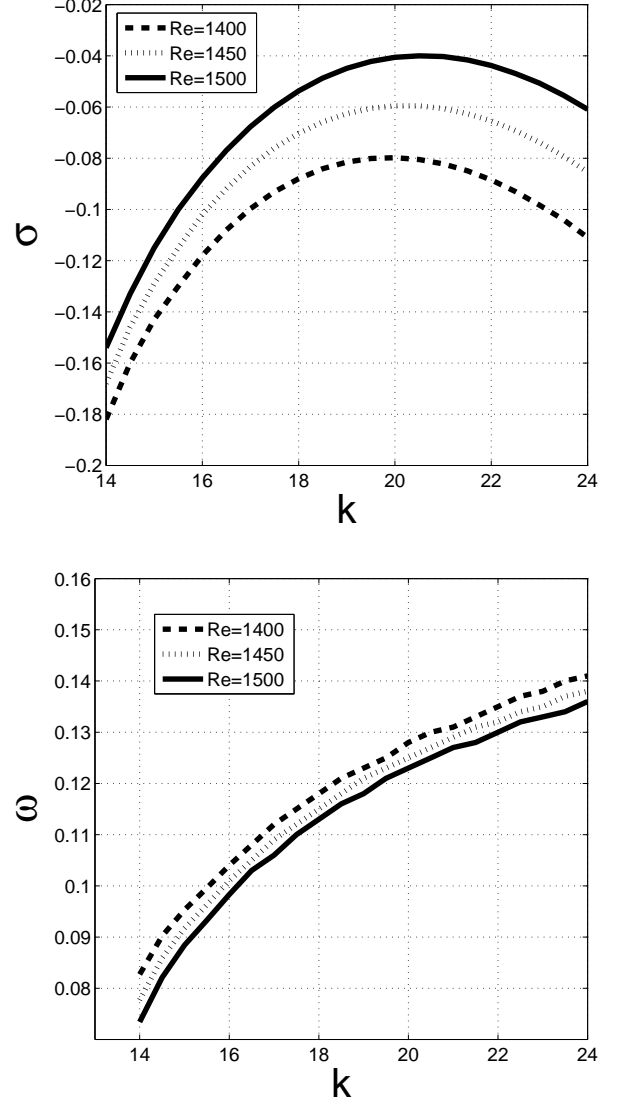

FIG. 18: Growth rates (top) and angular frequency (bottom) of the second less stable mode T2 versus k for different Reynolds numbers in the *CCavity*.

mode with zero-frequency exists in the *CCavity*, but is stable at the considered Reynolds number. For example, for the case: at Re = 1500 and $k = 21$, the stationary mode (without frequency) shows a decay rate of $\sigma = -0.154$. In this cavity, a travelling mode dominates the instability and the critical Reynolds and wavenumber values. One may conclude that rounding the corner provides stabilisation for the stationary mode, which was the most unstable in the *PCavity*. The stabilisation of the stationary mode enables larger Reynolds before the travelling mode T1 for the *CCavity* becomes unstable.

According to these results, the parameter that controls the change from two to three-dimensionality for the *CCavity* are well defined. Above Re_c, a three-dimensional simulation, in which $L_z = 2\pi/k_c$ is chosen according to the present theoretical results, will initially show exponential amplification of mode T1, leading to departure from the two-dimensional steady-state solution.

Similarly to what happens in the square cavity and the *PCavity*, see [49], most activity takes place in the neighbourhood of the left rounded wall of the cavity, which can be identified with the $x = 0$ wall of the square cavity (the lid leading edge). Another important similarity with the square cavity is that, when the spatial structure of the eigenfunctions of the three most unstable *CCavity* modes are compared, very few qualitative differences are found, see figure 21.
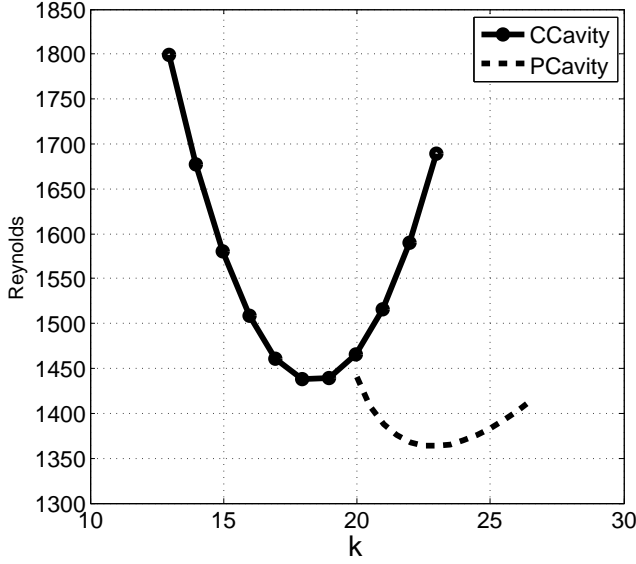
FIG. 19: Neutral stability curve for the *CCavity*(solid line) and *PCavity*(dotted line) using regularised boundary conditions.

The real parts of the direct and adjoint most unstable eigenmode, corresponding to the axial components, and the structural sensitivity of the *CCavity* are shown in figure 22. The adjoint mode presents again an almost symmetric structure compared to the direct and minimum overlap can be observed in the axial component. However, the overlap can be accurately computed using the structural sensitivity (wavemaker region), see figure 22. According to figure 22 the most sensitive region is located in the upper moving wall and cannot be separated in two blocks corresponding to the corners, as observed in the *PCavity*. This is a remarkable difference that shows that the most sensitive region changes its structure when corners are removed. Making the same comparison with the product of the direct and adjoint modes of the square lid driven cavity performed by [24], we confirm significant changes in the structural sensitivity that is now confined to the lid centre region and not to the left corner (leading edge of the cavity).

As in the previous *PCavity*, the results obtained by the global analysis are confirmed using DNS. For this cavity, we again observe very good agreement, as shown in figures 23 and 24. During the linear growth, we again compare the DNS solution on plane to the combined flow resulting when the base flow state is superposed by the scaled unstable mode. Views of this superposition are shown in figure 23 for two orthogonal planes at constant x=-0.35 and y=0.25 (as before), and located near the $\tilde{w}$ perturbation. Stability analysis and DNS results agree very well. Figure 13 shows the temporal evolution of the W-velocity. The growth rate measured in the DNS
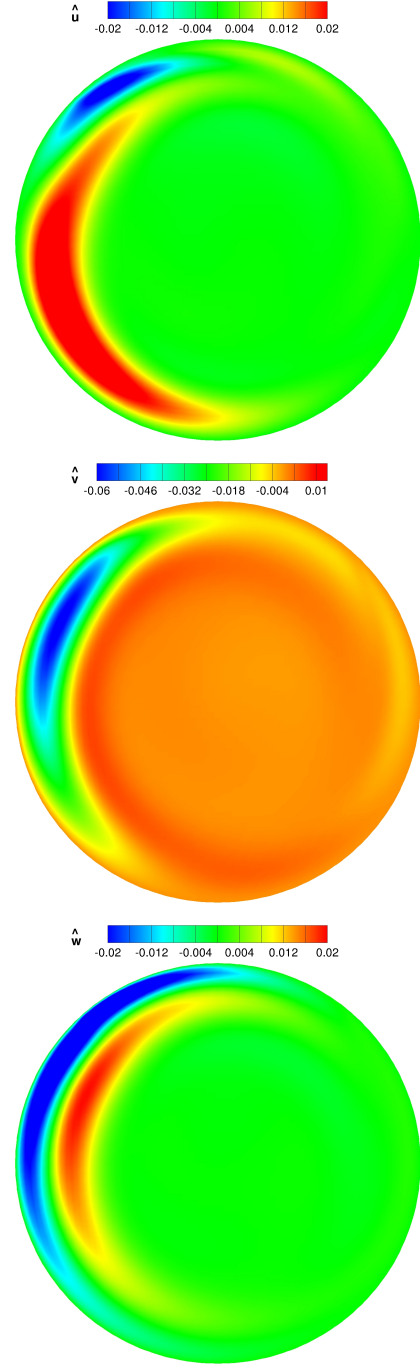

FIG. 20: Velocity perturbation amplitudes (real parts) of the most unstable mode T1 for the *CCavity* at Re=1500 and $k = 19$. Top: $\hat{u}$, middle: $\hat{v}$ and bottom: $\hat{w}$.

computation $\sigma \approx 0.03$ compares well with the stability results $\sigma = 0.0203$ at $Re = 1500$ and $k = 19$ and a dominant frequency observed in the DNS $\omega \approx 0.3$ for the unstable mode present in this cavity is not far from the corresponding stability analysis result $\omega = 0.248$.

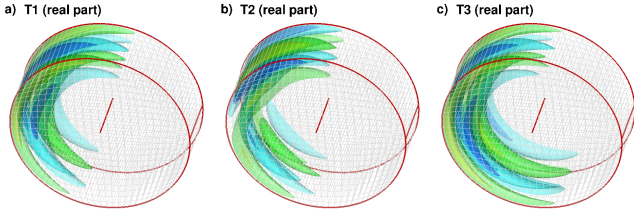The main hypothesis of this work is confirmed by

FIG. 21: Spatial distribution of the axial velocity perturbation of the three most unstable eigenmodes (T1, T2, T3) in the *CCavity* at $Re = 1500$ and $k = 19$. The eigenvalues are
$(\sigma, \omega) = (2.0257 \times 10^{-2}, 6.5999 \times 10^{-2}), (-4.4892 \times 10^{-2}, 1.1836 \times 10^{-1}), (-2.7664 \times 10^{-2}, 8.3931 \times 10^{-2}),$
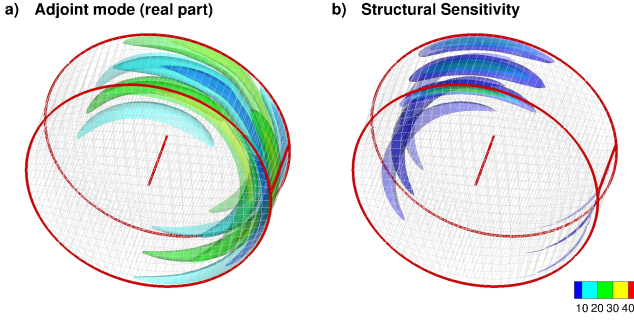

FIG. 22: *CCavity* at $Re = 1450$ and $k = 18$: a) Spatial distribution of the axial velocity perturbation of the adjoint most unstable eigenmode (associated to the direct mode S1) and b) corresponding structural sensitivity (wavemaker region).

the DNS computations, and the presence of corners reduces the critical stability of the cavity or that rounded geometries present enhanced stability.

V. CONCLUSIONS

The critical stability of the incompressible flow in two different lid-driven circular cavities has been increased once the corners have been partially or totally removed when compared to the classical square cavity. A first geometry, where only two corners are removed provide a critical mode at $Re_{crit} = 1362$ and $k_{crit} = 25$, which shows a critical Reynolds that doubles the Re_{crit} of the square lid driven cavity. In a second cavity, where all corners were removed and the external movement is applied tangentially along the curved boundary, the critical Reynolds number is even higher when compared to the first case.
Structural sensitivity iso-maps (i.e. wavemaker regions) confirm that the cavity corners play a relevant role in the generation of 3D instabilities.
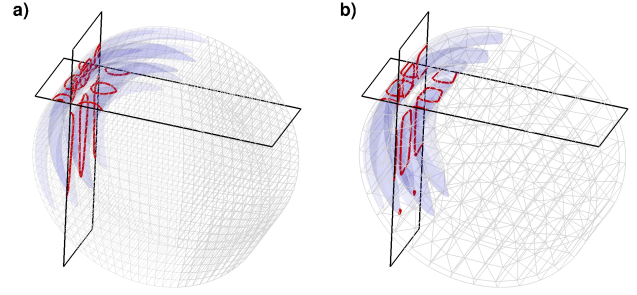To validate these results a spectral element DNS

FIG. 23: Superposition of the base flow and the arbitrarily scaled critical mode for $Re_c = 1500$ and $k_c = 19$ for one wavelength of the flow in the *CCavity*: a) linear stability analysis and b) DNS simulation. The cross-sections shown are taken at $x = -0.35$ and $y = 0.25$.
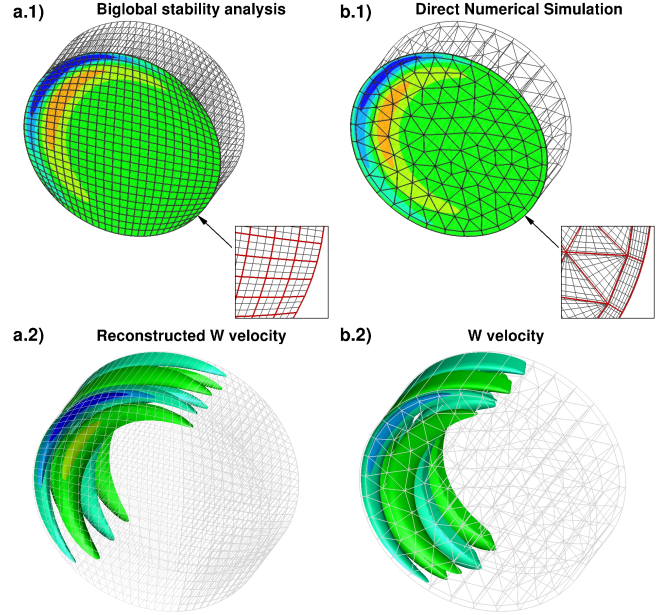

FIG. 24: Comparison between the W-velocity axial velocity perturbation of the *CCavity* at $Re = 1500$ and $k = 19$: a) the linear stability analysis and b) DNS simulation. Contour maps (top) and iso-surfaces (bottom).

computation has been used. The numerical results are in good agreement with the DNS observations of the supercritical flow. The critical wavenumber and the DNS supercritical flow pattern of the less stable mode of the *PCavity* are consistent with the wavenumber and structure of the critical mode obtained from the linear stability analysis. Regarding the *CCavity*, all critical parameters are also in good agreement. The critical modes discovered in these circular cavities as well as the

critical parameters are noticeably different to the critical modes observed in the classical square lid-driven-cavity problem.

VI. ANNEX

In this annex, we include convergence studies for the stability analysis and Direct Numerical Simulations.

First, we summarise in table IV a polynomial order P-convergence test for both cavities at supercritical Reynolds numbers. As the final eigenvalue is the result of two relevant computations, first the base flow calculation and then the eigenvalue calculation, the convergence is not completely monotonic, but the results are reasonably converged.

TABLE IV: Convergence table for different polynomial orders P direct analysis for the two cavities analysed.

P	$PCavity$ $Re = 1400$ $k = 23$ Mode S1 (σ, ω)	$CCavity$ $Re = 1500$ $k = 19$ Mode T1 (σ, ω)
3	(0.016019 , 0.00000)	(0.020257 , 0.24816)
6	(0.015879 , 0.00000)	(0.020163 , 0.24828)
8	(0.015914 , 0.00000)	(0.020107 , 0.24825)
10	(0.015903 , 0.00000)	(0.020095 , 0.24823)

Second, the DNS resolution is tested by doubling the maximum spanwise length (or halving the minimum wavenumber k that may be captured by the DNS) whilst maintaining the spatial discretisation in the axial direction: we use eight Fourier planes. Figure 25 shows minor differences between resolutions, which indicate convergence for DNS simulations and both cavities.
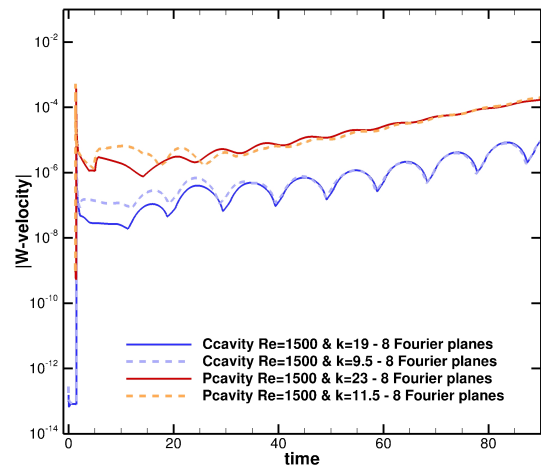

FIG. 25: Direct Numerical Simulation converge for the temporal evolution for the absolute value of the spanwise velocity component (W-velocity) monitored at $(x/d, y/d, z/d) = (0.1, 0.1, 0.0)$. $PCavity$ at $Re = 1500$ for $k = 23$ (solid red) and $k = 11.5$ (dashed orange). $CCavity$ at $Re = 1500$ for $k = 19$ (solid blue) and $k = 9.5$ (dashed light blue).

[1] S. Albensoeder and H. C. Kuhlmann. Linear stability of rectangular cavity flows driven by anti-parallel motion of two facing walls. *Journal of Fluid Mechanics*, 458:153–180, 2002.

[2] S. Albensoeder, H. C. Kuhlmann, and H. J. Rath. Multiplicity of steady two-dimensional flows in two-sided lid-driven cavities. *Theorical and Computational Fluid Dynamics*, 14:223–241, 2001.

[3] S. Albensoeder, H. C. Kuhlmann, and H. J. Rath. Three-dimensional centrifugal-flow instabilities in the lid-driven-cavity problem. *Physics of Fluids*, 13:121–135, 2001.

[4] D. Barkley, H.M. Blackburn, and S.J. Sherwin. Direct optimal growth analysis for timesteppers. *International Journal for Numerical Methods in Fluids*, 57(9):1435–1458, 2008.

[5] V. B. L. Boppana and J. S. B. Gajjar. Global flow instability in a lid-driven cavity. *International Journal of Numerical Methods in Fluids*, 62(8):827–53, 2010.

[6] G. A. Bres and T. Colonius. Three-dimensional instabilities in compressible flow over open cavities. *Journal of Fluid Mechanics*, 599:309–339, 2008.

[7] A. Brezillon, G. Girault, and J.M. Cadou. A numerical algorithm coupling a bifurcating indicator and a direct method for the computation of hopf bifurcation points in fluid mechanics. *Computers and Fluids*, 39(7):1226 – 1240, 2010.

[8] O.M.F. Browne, G. Rubio, E. Ferrer, and E. Valero. Sensitivity analysis to unsteady perturbations of complex flows: a discrete approach. *International Journal for Numerical Methods in Fluids*, 76(12):1088–1110, 2014.

[9] C.D. Cantwell, D. Moxey, A. Comerford, A. Bolis, G. Rocco, G. Mengaldo, D. De Grazia, S. Yakovlev, J.-E. Lombard, D. Ekelschot, B. Jordi, H. Xu, Y. Mohamied, C. Eskilsson, B. Nelson, P. Vos, C. Biotto, R.M. Kirby, and S.J. Sherwin. Nektar++: An open-source spectral/element framework. *Computer Physics Communications*, 192:205 – 219, 2015.

[10] J.M. Chomaz. Global instabilities in spatially developing flows: non-normality and nonlinearity. *Annual Review of Fluid Mechanics*, 37(1):357–392, 2005.

[11] V. Citro, F. Giannetti, L. Brandt, and P. Luchini. Linear three-dimensional global and asymptotic stability analysis of incompressible open cavity flow. *Journal of Fluid Mechanics*, 768:113–140, 004 2015.

[12] J. H. Darr and S. P. Vanka. Separated flow in a driven trapezoidal cavity. *Phys. Fluids* A, 3:385–392, 1991.

[13] J. de Vicente, D. Rodriguez, V. Theofilis, and E. Valero. Stability analysis in spanwise-periodic double-sided lid-driven cavity flows with complex cross-sectional profiles. *Computers and Fluids*, 43(1):143 – 153, 2011.

[14] Y. Ding and M. Kawahara. Linear stability of incom-

pressible flow using a mixed finite element method. *Journal Computationa Physics*, 139:243–273, 1998.

[15] F. F. Gomez, S. Le Clainche, P. Paredes, M. Hermanns, and Theofilis V. Four decades of studying global linear instability: Progress and challenges. *AIAA Journal*, 50(12):2731–2743, 2012.

[16] E. Ferrer. *A high order Discontinuous Galerkin - Fourier incompressible 3D Navier-Stokes solver with rotating sliding meshes for simulating cross-flow turbines.* PhD thesis, University of Oxford, 2012.

[17] E. Ferrer, J. de Vicente, and E. Valero. Low cost 3d global instability analysis and flow sensitivity based on dynamic mode decomposition and high-order numerical tools. *International Journal for Numerical Methods in Fluids*, 76(3):169–184, 2014.

[18] E. Ferrer, D. Moxey, R.H.J. Willden, and S. Sherwin. Stability of projection methods for incompressible flows using high order pressure-velocity pairs of same degree: Continuous and discontinuous galerkin formulations. *Communications in Computational Physics*, 16(3):817–840, 2014.

[19] E. Ferrer and R. H. J. Willden. A high order Discontinuous Galerkin Finite Element solver for the incompressible Navier-Stokes equations. *Computers and Fluids*, 46(1):224–230, 2011.

[20] E. Ferrer and R. H.J. Willden. A high order discontinuous Galerkin - Fourier incompressible 3D Navier-Stokes solver with rotating sliding meshes. *Journal of Computational Physics*, 231(21):7037–7056, 2012.

[21] P.H. Gaskell, H.M. Thompson, and M.D. Savage. A finite element analysis of steady viscous flow in triangular cavities. In *Proceedings of the Institution of Mechanical Engineers Part C-Journal of Mechanical Engineering Science*, volume 213, pages 263–276, 1999.

[22] U. Ghia, K.N. Ghia, and C.T. Shin. High-re solutions for incompressible flow using the Navier-Stokes equations and a multigrid method. *Journal of Computational Physics*, 48:387–411, 1982.

[23] F. Giannetti and P. Luchini. Structural sensitivity of the first instability of the cylinder wake. *Journal of Fluid Mechanics*, 581:167–197, 2007.

[24] F. Giannetti, P. Luchini, and L. Marino. Characterization of the three-dimensional instability in a lid-driven cavity by an adjoint based analysis. In *Proceedings of the 7th IUTAM Symposium on Laminar-Turbulent Transition*, pages 165–170, Stockholm, Sweden, 2010. Springer.

[25] G.J. Chandler GJ, M.P. Juniper, J.W. Nichols, and P.J. Schmid. Adjoint algorithms for the navier–stokes equations in the low mach number limit. *Journal of Computational Physics*, 231(4):1900–1916, 2012.

[26] L. M. Gonzalez, M. Ahmed, J. Kühnen, H. C. Kuhlmann, and V. Theofilis. Three-dimensional flow instability in a lid-driven isosceles triangular cavity. *Journal of Fluid Mechanics*, 675:369–396, 5 2011.

[27] L. M. Gonzalez and R. Bermejo. A semi-langrangian level set method for incompressible navier-stokes equations with free surface. *International Journal of Numerical Methods in Fluids*, 49:1111–1146, 2005.

[28] L. M. Gonzalez, V. Theofilis, and R. Gómez-Blanco. Finite-element numerical methods for viscous incompressible BiGlobal linear instability analysis on unstructured meshes. AIAA *Journal*, 45:840–854, 2007.

[29] M. Hinatsu and J. H. Ferziger. Numerical computation of unsteady incompressible flow in complex geometry using a composite multigrid technique. *International Journal of Numerical Methods in Fluids*, 13(8):971–997, 1991.

[30] M.C. Iorio, L.M. Gonzalez, and E. Ferrer. Direct and adjoint global stability analysis of turbulent transonic flows over a NACA0012 profile. *International Journal for Numerical Methods in Fluids*, 76(3):147–168, 2014.

[31] R. Jyotsna and S. P. Vanka. Multigrid calculation of steady, viscous flow in a triangular cavity. *Journal Computationa Physics*, 122:107–117, 1995.

[32] H.C. Kuhlmann and S. Albensoeder. Stability of the steady three-dimensional lid-driven flow in a cube and the supercritical flow dynamics. *Physics of Fluids*, 26(2):024104, 2014.

[33] E. Leriche, S. Gavrilakis, and M. O. Deville. Direct simulation of the lid-driven cavity flow with chebyshev polynomials. In K. D. Papailiou, editor, *Proc. 4th European Computational Fluid Dynamics Conference*, volume 1(1), pages 220–225. ECCOMAS, 1998.

[34] P. Luchini and A. Bottaro. Adjoint equations in stability analysis. *Annual Review of Fluid Mechanics*, 46:493–517, 2014.

[35] O. Marquet, D. Sipp, and L. Jacquin. Sensitivity analysis and passive control of cylinder flow. *Journal of Fluid Mechanics*, 615:221–252, 2008.

[36] W. D. McQuain, C. J. Ribbens, C.-Y. Wang, and L.T. Watson. Steady viscous flow in a trapezoidal cavity. *Computers and Fluids*, 23:613–626, 1994.

[37] F. Meseguer-Garrido, J. de Vicente, E. Valero, and V. Theofilis. On linear instability mechanisms in incompressible open cavity flow. *Journal of Fluid Mechanics*, 752:219–236, 2014.

[38] C. W. Oosterlee, P. Wesseling, A. Segal, and E. Brakkee. Benchmark solutions for the incompressible Navier-Stokes equations in general coordinates on staggered grids. *International Journal of Numerical Methods in Fluids*, 17:301–321, 1993.

[39] C. Y. Perng and R. L. Street. A coupled multigrid-domain-splitting technique for simulating incompressible flows in geometrically complex domains. *International Journal of Numerical Methods in Fluids*, 13(3):269–286, 1991.

[40] M. Poliashenko and C.K. Aidun. A direct method for computation of simple bifurcations. *Journal of Computational Physics*, 121(2):246 – 260, 1995.

[41] C. J. Ribbens, C.-Y. Wang, L. T. Watson, and K. A. Alexander. Vorticity induced by a moving elliptic belt. *Computers and Fluids*, 20:111–119, 1991.

[42] C. J. Ribbens, L. T. Watson, and C.-Y. Wang. Steady viscous flow in a triangular cavity. *Journal Computationa Physics*, 112:173–181, 1994.

[43] Y. Saad. Variations of Arnoldi's method for computing eigenelements of large unsymmetric matrices. *Lin. Algebra. Appl.*, 34:269–295, 1980.

[44] R. Schreiber and H.B. Keller. Driven cavity flows by efficient numerical techniques. *Journal of Computational Physics*, 49:310–333, 1983.

[45] P. N. Shankar and M. D. Deshpande. Fluid mechanics in the driven cavity. *Annuual Review of Fluid Mechanics*, 32:93–136, 2000.

[46] V. Theofilis. Globally unstable basic flows in open cavities. In *6th AIAA Aeroacoustics Conference and Exhibit, Lahaina, HI, USA*. AIAA Paper 2000-1965, 2000.

[47] V. Theofilis. Advances in global linear instability analysis

of nonparallel and three-dimensional flows. *Prog. Aero. Sci.*, 39:249–315, 2003.

[48] V. Theofilis. Global linear instability. *Annual Review of Fluid Mechanics*, 43(1):319–352, 2011.

[49] V. Theofilis, P.W. Duck, and J. Owen. Viscous linear stability analysis of rectangular duct and cavity flows. *Journal Fluid Mechanics*, 505:249–286, 2004.

[50] M. Vynnycky and S. Kimura. An investigation of

recirculating flow in a driven cavity. *Physic of Fluids*, 6:3610, 1994.

[51] Z.J. Wang, R. Fidkowski, K.and Abgrall, F. Bassi, D. Caraeni, A. Cary, H. Deconinck, R. Hartmann, K. Hillewaert, H.T. Huynh, N. Kroll, G. May, P.O. Persson, B. van Leer, and M. Visbal. High-order cfd methods: current status and perspective. *International Journal for Numerical Methods in Fluids*, 72(8):811–845, 2013.